Nanoscale Control of Molecular Self-Assembly Induced by Plasmonic Hot-Electron Dynamics

Sabrina Simoncelli,[1‡]* *Yi Li,*[1‡] *Emiliano Cortés,*[1] *Stefan A. Maier*[1,2]

[1]The Blackett Laboratory, Department of Physics, Imperial College London, London SW7 2AZ, United Kingdom.

[2]Chair in Hybrid Nanosystems, Faculty of Physics, Ludwig-Maximilians-Universität München, 80799 München, Germany.

* E-mail: s.simoncelli@imperial.ac.uk

ABSTRACT. Self-assembly processes allow designing and creating complex nanostructures using molecules as building blocks and surfaces as scaffolds. This autonomous driven construction is possible due to a complex thermodynamic balance of molecule-surface interactions. As such, nanoscale guidance and control over this process is hard to achieve. Here we use the highly localized light-to-chemical-energy conversion of plasmonic materials to spatially cleave Au-S bonds on pre-determined locations within a single nanoparticle, enabling a high degree of control over this archetypal system for molecular self-assembly. Our method offers nanoscale precision and high-throughput light-induced tailoring of the surface chemistry of individual and packed nano-sized metallic structures by simply varying wavelength and polarization of the incident light. Assisted by single-molecule super-resolution fluorescence

microscopy, we image, quantify and shed light onto the plasmon-induced desorption mechanism. Our results point towards localized distribution of hot electrons, contrary to uniformly distributed lattice heating, as the mechanism inducing Au-S bond breaking. We demonstrate that plasmon-induced photo-desorption enables sub-diffraction and even sub-particle multiplexing. Finally, we explore possible routes to further exploit these concepts for the selective positioning of nanomaterials and the sorting and purification of colloidal nanoparticles.

Keywords: plasmonics, hot-electrons, super-resolution, dynamic self-assembly, multiplexing, nanoscale precision.

Self-driven assembly of thiolated molecules onto metals offers a direct route to tailor the surface chemistry and functionalities of nanomaterials, cementing the bottom-up hierarchal construction of complex nanosystems.[1,2] The robust metal-sulfur bond formation drives the self-assembly process and the strength of van der Walls interactions between molecules stabilize and order the molecular layer, hindering their diffusion and turning them amenable to pattern surfaces properties by almost free election of their terminal group.[3–5] There is a wide variety of either bio-functional molecules (DNA, proteins, amino acids) or inorganic molecules, complexes and polymers that intrinsically have or can be further modified with a thiol group. As such, thiols are the natural workhorse molecular linkers in various fields of nanoscience including molecular electronics, catalysis, sensing and medical therapy, among many others.[3,6] Given the technological importance of these surface chemistry processes, controlling them down to the nanometer scale can impact in various fields of current nanoscience and nanotechnology. At the moment, there are no simple and easy-to-implement strategies to '*in-situ*' control the self-assembly process down to the sub-nanoparticle level. Some advances on this direction, although

limited in achieving sub-nanoparticle precision, include techniques such as micro-contact printing,[7] direct laser patterning[8] and electrochemical stripping.[9] These micro-scale pattering self-assembly techniques are deceptively simple; their spatial resolution is highly dependent upon fabrication of stamps and/or transfer conditions, the laser beam size and power or the size of the metallic micro-electrodes, respectively. In this regard, Mirkin *et al*. pioneered on achieving highly reproducible nanoscale manipulation (~ 50 nm) of alkanethiols self-assembly with the introduction of dip-pen nanolithography.[10] Dip-pen nanolithography exploits the capillary action between an atomic force microscope tip and a gold substrate to produce multi-molecule patterns, withal, it tends to be technically involved to implement and it is a time-consuming 'bottom up' process. Alternative methods to spatially control the surface chemistry of nano-sized structures and colloids could revolution our current abilities to produce multi-functional nano-materials.

It is well known that thiol-release from metal surfaces can be induced by temperature, light, voltage and chemical reagents.[3–5,11,12] However, none of these routes have proven specificity and sub-diffraction spatial control over this process. To this end, deep understanding of the reactivity of the Au-S bond under external stimuli could provide interesting possibilities for tailoring functionalities and the manipulation of nanostructures. In particular, the enhanced absorption of photons in metal nanostructures in comparison to bulk metal surfaces and the subsequent excitation and non-radiative decay of surface plasmon resonances offers exciting opportunities for light-into-chemical energy conversion.[13–16] Plasmon-enhanced photo-catalytic processes, such as CO oxidation, H_2 dissociation, nitro to amino conversion and water splitting, among others, have been successfully achieved.[17–19] DNA origami assembled with plasmonic nanoparticles have been recently used for creating tunnel junctions for redox chemistry[20] or

nanoscale energy manipulation.[21] Photo-release of thiolated single-stranded DNA molecules from gold nanoparticles was also reported.[11,12] The vital use of ultrafast laser excitation bridges the knowledge of femtosecond dynamics of chemical bonds,[22] in particular at the metal surfaces[23] with multi-step processes. Although a lot is known about the photophysics of electron-induced interfacial desorption and chemical conversion[24] as well as plasmon-induced photochemical processes, the potential to engineer spatial and/or chemical selectivity has not yet been fully exploited.[25–27] Here, we take advantage of the plasmon-mediated light-induced cleavage of thiol molecules on the surfaces of gold nanostructures followed by ligand-replacement for '*in-situ*' nano-localized patterning. We use super-resolution imaging to demonstrate the hot-electron driven nature of the process. The confined and tunable hot-electrons localization in plasmonic materials offers greater degree of freedom to tailor surface chemistry self-assembly. Notably, understanding plasmonic–photonic interactions allows for the predesign of specific functionalities on either sub-particle surfaces or nanosized elements of complex metallic nanoclusters. Our results can be exploited for the design, fabrication, and applications of functional platforms in the nanoscale regime.

Results

Figure 1a illustrates the concept of our simple yet arguably elegant plasmon-induced spatial functionalization approach. First, a monolayer of thiol reactive molecules is self-assembled on electron-beam patterned gold nanoantenna arrays. We use dark-field scattering spectroscopy and numerical simulations to determine the plasmon resonance wavelengths of each fabricated structure. Next, individual functionalized gold nanoantennas embedded in a microfluidic chamber are irradiated with a wavelength-tunable linearly polarized 180 fs pulsed laser. Due to the resonant energy transfer into electron cloud dipole oscillations, we would

expect an enhanced optical absorption on the nanoantenna element(s) parallel to the excitation polarization. Therefore, only the thiol molecules localized on the resonantly excited region of the nanoantenna are expected to detach from the surface, leaving it now accessible for further functionalization with another type of molecules. Finally, a second step of incubation is performed on the irradiated gold nanoantenna to selectively bind a different type of thiol-reactive probe to the bare elements. Automation of this procedure is easily achieved by combining the use of a fluidic chamber, for rapid fluid exchange, and of a nanopositioning piezo-stage to irradiate micro-sized arrays of nanostructures in a just a few seconds. As such, this approach can be extended to incorporate multiple functional groups with nano-sized precision on selective surfaces of plasmonic antennas by consecutive irradiation and incubation steps.

m-PAINT super-resolution imaging of molecular targets on metallic surfaces

To map the surface chemistry evolution of gold nanoantennas with sub-diffraction resolution, we adapt a point-localization-based super-resolution fluorescence technique, named DNA-PAINT (point accumulation for imaging in nanoscale topography).[28,29] DNA-PAINT employs transiently binding of short fluorescently labeled oligonucleotides (‘imager strands’) to complementary single-stranded DNA oligos (‘docking strands’) chemically coupled to a target object. Figure 1b shows the scheme of the super-resolution metallic DNA-PAINT (m-PAINT) imaging technique. First, docking strands, chemically coupled to a supplementary hydrophilic PEG unit in the form of hexaethylene glycol, are docked to the metallic surface through a mercaptohexyl linker (Figure 1b, i).[30] The introduction of such a PEG moiety optimizes the separation distance between the fluorophores and the metallic surface to ~ 7 nm and as such, it diminishes the spatial fluorescence quenching effects on metals.[31,32] Additionally, we choose a backfilling molecule (6-mercapto-1-hexanol, MCH) to help maintaining the availability of the

ssDNA docking molecules by blocking binding sites and thus preventing unspecific binding.[33] Finally, the density of docking strands on the surface of the gold nanoantennas are comprehensively optimized by tuning the assembly time, thiolated (hence docking) ssDNA concentration, and salt concentration. From reductive electrodesorption measurements we estimate a ratio of ~ 1:160 between ssDNA and MCH molecules (see Section 1 of the Supporting Information and Figure S1), which results in ~ 1 binding event per antenna per 0.8 s (eight frames). This number of events was sufficient to reconstruct in 20,000 frames an accurate representation of the nano-sized objects as well as the localization of different types of target molecules over the surface of the nanoantennas (Figure 1b, iv-ix). To avoid mislocalization of the docking strands due to light coupling of the emitter to the optical density of states of the plasmonic antenna, we labeled the imager strands with a fluorophore (Atto 655) whose absorption and emission spectra are decoupled and blue shifted with respect to the plasmonic modes of all the nanoantennas, thus approaching to the free-space emission condition.[34,35] We evaluated the imaging performance of m-PAINT by visualization of a sub-diffraction six-leg gold nano-assembly structure (Figure 1b, iv). The individual super-resolved images show a clear increase in spatial resolution from the diffraction-limited representation (Figure 1b, v-viii). Comparing the SEM images and the super-resolved images of individual six-leg structures demonstrates that we can successfully resolve metallic nanostructures using m-PAINT. To account for the fact that more localization events render a better-defined nanoantenna image, we overlaid super-resolution images of 36 individual gold nanostructures using a translation registration algorithm (see Methods, Figure S2 and Figure 1b, ix). The high-density super resolution image of the six-leg structure accurately represents the geometry of the fabricated one

(Figure 1b, iii). In fact, imaging technique renders a localization precision of ~8 nm and it can perfectly resolve the smallest features of our fabricated structures (Figure S3).

Selection rules for controlling the nano-localized Au-S desorption

We first tested the performance of the plasmon-selective functionalization procedure on trimer gold nanorods. The wavelength of irradiation was chosen to excite the longitudinal plasmonic mode of the nanorods (Figure S4). Figure 1c shows the m-PAINT super-resolution average images of nanotrimer arrays before (i) and after (ii) irradiation with a 950 nm linearly polarized femtosecond pulsed laser. After laser irradiation, we only observed DNA binding fluorescent events in the nanorods whose orientation is not parallel to the laser polarization. Note, however, that the spot size of the ultrafast laser was ~2.7 μm, measured *via* determining its point spread function (PSF), meaning that the whole nanotrimer structure is being irradiated. This indicates that only the organothiol molecules localized on the surface of the resonantly excited nanorod were selectively desorbed after irradiation (Figure 1c, ii). The reproducibility of the technique is further evidenced by the super-resolution images of 28 individual irradiated nanoantennas (Figure S5). We achieved bi-functionalization in a sub-diffraction limited area by incubating the sample with a different type of thiol-labeled docking strand (P_2). The second round of super-resolution imaging (imaging strand P_2*) demonstrates that our plasmon-selective functionalization approach is a rapid method for tailoring the chemical surface of plasmonic nanostructures with sub-diffraction resolution (Figure 1c, iii). This experiment also confirms that the integrity of the excited nanorod is maintained after irradiation (*i.e.* gold antennas do not melt). We also demonstrated that when the trimer is resonantly excited, we can selectively desorb and re-functionalize thiol-labeled molecules from any desired rod of the nanostructure just by rotating the polarization of the incident light (Figure S6).

We generalize this idea to complex gold nanoclusters, where on-demand patterning requires both wavelength and polarization selection rules of the incident light. Figure 2a shows the two building blocks for our demonstration nanoclusters, whose resonances are well separated at 835 nm and 1040 nm (Figure 2b). We first assess the specificity provided by excitation wavelength on gold nanoclusters composed of six nanorods. Figure 2g and 2h depict the metallic DNA-PAINT images of the six-leg nanostructures irradiated with two distinct wavelengths. The preferential desorption of the thiol labeled docking strand P_1 from the resonantly excited nanorods indicates that spectral differences provide an additional efficient way to tune the surface chemistry of packed nanoclusters, in addition to polarization as demonstrated in Figure 1. We then constructed a letter pattern 'ICL' (abbr. of Imperial College London), shown in Figure 2e, for multiplexing at two wavelengths and two polarizations in a structure where plasmonic near-field coupling may hinder the general use of our technique. Even though the plasmonic resonances between the two building blocks of the 'ICL' design couple (Figure S8, vertical polarization), Figure 2i and 2j shows Au-S desorption with high selectivity. Thus, our experimental results indicate that near-field cross-talk among the nanorods does not contribute significantly to the general Au-S desorption mechanism.

Spatial and temporal study of Au-S photo-desorption mechanism

In order to assess the extent of applicability of our plasmon-selective surface chemistry modification approach, we next investigated the Au-S desorption mechanism. Plasmon-induced Au-S photo-desorption can be triggered by one of the two general mechanisms facilitated by the dominant non-radiative plasmon decay channels: localized heating of the surrounding medium or 'hot'-carrier-driven chemical reactions.[11,12,17,36] Following femtosecond laser irradiation, surface plasmons decay into anisotropic distributions of hot electrons (or holes) within ~ 40 fs.[18,37–39]

While these energetic electrons are localized in regions of dense resistive losses of the particle, they later (on a time scale of ~800 fs) redistribute their energy *via* electron-phonon scattering, which leads to a uniform lattice temperature distribution due to reasonable high thermal conductivity and longer response time (see Section 2 of the Supporting Information).[18,40] Therefore, selective control over the spatially localized chemistry of a single plasmonic nanoantenna can only be achieved prior to this electron-lattice thermalization.[19] To straightforwardly assess the origin of the gold-thiol desorption mechanism, we designed a branched plasmonic antenna, such as a 'L' shape letter, capable of differentiating between the two photo-driven processes (Figure 3a-c).

Figure 3d-f shows the super-resolved fluorescence images of 'L' connected gold nanoantennas before and after irradiation. The spatially resolved images reveal that depending on the polarization of the incident laser only molecules localized either on the horizontal or on the vertical leg of the 'L' structure desorbed (Figure S9). Furthermore, it is worth pointing out that considering the radios of curvature of our L-shaped nanoantennas (> 5 nm) we do not expect to have different adsorption strengths for thiol molecules adsorbed on the knots (connection point of the two legs) compared to the legs.[41] These results are in line with a hot-electron initiated process, in which asymmetric distribution of resistive losses induces localized reductive desorption of the thiolated molecules. The ultrafast generation of hot electrons and posterior lattice heating (phonons) are calculated using a dual-hyperbolic two-temperature model, which is semi-classical yet suitable for high intensity and short pulse laser heating. The details of the modeling and physical parameters are described in the Section 2 of the Supporting Information. Based on this two-temperature model, the maps of the lattice temperature and the conduction electrons density of the 'L' shaped nanoantenna shows that while the temperature is

homogenously distributed on our L-shape structure, the generated hot-electrons are highly localized in the leg parallel to the irradiation polarization. In our numerical simulations, we have taken the electronic and lattice heat conduction and heat capacitance into the consideration, which shows that the L-shape structure operates as an entire unit. Notably, the intrinsic short lifetime of hot electrons offers high degree of confinement to tailor sub-particle surface chemistry (Figure 3e and 3f). Contrary to excited carriers, the uniform nanosecond lattice heating has no spatial resolution for thermally induced desorption in single nanoantennas. Furthermore, the kinetics for thermal induced thiol-release should be hindered on this timescale.[12] Tunneling spectroscopy experiments of thiolated SAMs on Au(111) have recently shown that in the range of ~1.2 to ~1.4 eV above the Fermi level there exist unoccupied states, derived from the Au–S hybridization and induced by the strong coupling of S to the Au substrate.[42,43] This range of energies perfectly match with the energy of the photons employed in our experiments, suggesting that those states could be involved in our hot-electrons induced desorption process.

Another evidence, which points to a hot-electron-driven-mechanism, is the nearly linear dependence of the Au-S release on laser intensity (Figure 3g).[17] Contrary to a thermal activated process, where a Heaviside step function is expected once the desorption temperature is reached,[44] we observed a monotonic increase in the desorption percentage with increasing the laser power.[45] This is consistent with a hot-electron-initiated bond dissociation reaction, where the number of generated hot carriers has a positive relationship with the photon flux. Moreover, tracking the number of localizations in the reactive element of the antenna as a function of incident laser power allows quantification of desorption events, which is in line with the number of hot-electrons able to react. As it can be seen in Figure 3g i-iv, the horizontal rod of the antenna becomes dimmer as the irradiation power of the horizontal-polarized beam is increased

(*i.e.* increasing the number of desorbed molecules and leading to a reduction in the number of localizations).[45] We do not observe preferential plasmon-induced reaction in the corners of the nanoantenna with respect to the flat planar sections of the structure, in line with previous results by our group for antennas that do not possess sharp tips or edges.[19] By correlating the total number of molecules self-assembled on a single rod of the structure and the power needed to desorb them it is possible to derive the number of molecules released per pulse of light. From electrochemical measurements (see Section 1 of the Supporting Information) we obtained the surface coverage of the SAM, accounting for ~1×10^5 molecules per rod. In this way, we estimate that 10 Au-S bonds are cleaved per pulse of light for a fluence of 1.7 mJ cm^{-2}, a similar figure to the one reported for hot-electron induced H_2 dissociation in Al-Pd nanoantennas.[46]

Our experimental results on the anisotropic desorption of thiolated molecules (Figure 3e-f and Figure S9) and its nearly linear power dependency (Figure 3g), combined with our theoretical simulations (Figure 3c and 3h), strongly suggests a hot-electron initiated process rather than a phonon driven reaction for the photo-desorption of thiol molecules on gold. However, we cannot simply exclude contributions of thermal effects, which might help hot-electron injection by lowering the activation barrier of the Au-S bond cleavage.

Applications of plasmon-guided ligand replacement

Finally, we show the versatility of the plasmon-selective functionalization procedure to, for example, guide the positioning of nano-objects at the nanoscale (Figure 4a). We start by functionalizing the nanoantennas with a self-assembled monolayer of MCH molecules followed by targeted MCH photo-desorption. Ligand replacement allows the self-assembly of thiolated biotin-terminal linkers at specific locations of the nanostructure – *i.e.* only at the places where

MCH was previously removed – which can further bind streptavidin coated gold nanoparticles. Figure 4b-e depict the preferential attachment of streptavidin coated 50 nm gold nanoparticles to one or two rods of the nanotrimer depending on the direction of the incident light in the initial removal process. Although further optimization is required to attain a more controllable nanoparticle binding, our results show the potential of using plasmon-selective desorption to enable hierarchical nanoparticles assembly.

This initial example is one out of many possible routes for exploration. Solution-based experiments for example should hold the wavelength-dependence selection rule while losing the polarization-control over the process. In this way, selective capping removal in a heterogeneous mixture of plasmonic colloids can be achieved (see Section 3 and Figure S11 of the Supporting Information). This proof of concept not only extends our findings to solution-based experiments but also demonstrates that in principle any thiolated molecule can be also selectively displaced, as the energy of the Au-S bond is nearly independent on the nature of the backbone chain.[3,47]

Conclusions

Here, we have described a simple, rapid and robust nanofabrication approach to control, with sub-diffraction precision, the surface chemistry of individual and clustered metallic nanoantennas. While continuous wavelength illumination of plasmonic nanostructures can induce chemical changes in the redox-active terminal groups of self-assembled monolayers of short molecules, ultrafast illumination enables cleavage of their anchor group.[11,19] This degree of chemical selectivity in photo-induced processes provides further possibilities for controlling reaction pathways.[48] Furthermore, we show that by exploiting the localization of hot-electron carriers we can selectively drive Au-S cleavage on individual strands of multi-element

nanoantennas by just varying the light polarization and the wavelength. Similar to dip-pen lithography,[10] our selective functionalization platform can be rapidly adopted to incorporate different functional groups (bio-molecules, inorganic complexes, polymers) on an array of nanoparticles and to even position other nano-sized components, such as nanoparticles or quantum dots, on any targeted region. The characteristics of our desorption/re-adsorption strategy and the single-molecule super-resolution fluorescence imaging approach provides direct evidence on the nanoscopic mechanism of plasmon-induced molecular desorption under femtosecond laser irradiation. We found that Au-S desorption is induced by localized hot electrons and that thermal-driven reactions can be ruled out.[11,12] The tunable anisotropic distribution of resistive losses provides a degree of surface-targeted specificity that could not be attained with thermal or electrical driven processes. Exploiting resistive losses at the sub-particle scale allows controlled and self-induced selective capping removal/replacement.

This level of selectivity can provide interesting opportunities for the synthesis of nanomaterials, where tight control of these parameters dictates the final shape and size of the nano-objects.[49] Our approach unlocks the use of ultrafast, spatially anisotropic features of plasmon-induced hot electrons for positioning and selective functionalization at the nanoscale.

Methods

Materials: Thiol-labeled and Atto 655 fluorescently modified single stranded DNA oligos were purchased from biomers.net GmbH (see Supporting Table 1). Glass coverslips were purchased from VWR. Sticky-Slide VI 0.4 slides were purchased from Ibidi. Remover 1165 and poly(methyl methacrylate) (PMMA) 950K A4 were purchased from Dow and Microchem, respectively. 6-Mercapto-1-hexanol (MCH) and Tris (carboxyethyl) phosphine hydrochloride

were purchased from Sigma-Aldrich (catalogue numbers: 451088 and C4706, respectively). Streptavidin functionalized gold nanoparticles were purchased from Nanopartz Inc. Self-assemble monolayer reagent for biotin terminate monolayer on gold surface was obtained from Sigma-Aldrich (catalogue number: 746622). Three buffers were used for sample functionalization and imaging: buffer A (10 mM TRIS-HCl, 1 M NaCl, pH = 7), buffer B (10 mM TRIS-HCl, 50 mM NaCl, pH = 7 and buffer C (5 mM TRIS-HCl, 10 mM $MgCl_2$, 1 mM EDTA, pH = 8).

Gold nanostructures fabrication and scanning electron microscopy imaging. Gold nanoantenna arrays with 3 μm pitch were fabricated on borosilicate glass coverslips using electron beam lithography (E-line, Raith GmbH). The substrate was first coated with poly(methyl methacrylate) (PMMA) 950K A4 at 3,000 r.p.m. for 60 s and then baked for 3 min at 180 °C. Following the film preparation, a conductive layer of Espacer 300Z (Showa Denko) was spin coated onto the sample. Nanostructures were defined into PMMA by an electron beam exposure at 20 keV. After patterning, the spacer was removed using deionized water, followed by an MIBK/IPA (1:3) based development procedure. The pattern was then cleaned by a plasma ash etch step (Femto, Diener Electronic GmbH, 7 s at 40% power). Chromium and gold were coated at 1.5 Å/s for 1.5 nm and 30 nm *via* thermal evaporation (Amod, Angstrom Engineering Inc), and a standard lift-off process with Remover 1165 (Microposit, Dow Electronic Materials) at 70 °C completed the fabrication process. To image the nanoantennas, 20 nm thin film of Espacer 300Z was coated onto the sample at 2,000 r.p.m. for 60 s, followed by a 60 s, 90 °C bake. For scanning electron microscopy imaging, we typically used an electron-beam energy of 10 keV, a beam aperture of 30 μm and a working distance of 10 mm.

Dark-field spectroscopy. Dark-field spectra of the scattering cross-sections of the antennas in air were measured with a diffractive grating and charge-coupled device camera cooled to 70 K. The plotted spectra are corrected for the system wavelength response (by measuring the cross section of a perfect reference white rough scatter) and also for dark and background counts. A dark field objective (Nikon LU Plan ELWD 100× NA 0.80) was used for both, to provide the incident illumination and to collect the scattered light.

Gold-sulfur functionalization. DNA functionalization of the previously fabricated gold nanoantenna arrays was performed as follows. First, the sample was thoroughly cleaned with isopropanol and water. Then, the sample was dried with nitrogen and left for 1.5 min in a UVO cleaner/oxidizer (Femto, Diener Electronic GmbH). The sample was mounted to a bottomless self-adhesive slide (sticky-Slide VI 0.4, Ibidi) which, has been previously plasma clean for 10 min, to form a flow chamber of six individual channels with inner volumes of ~ 30 µL each. Each channel was functionalized independently from the other. First, the channel was rinse with 100 µL of buffer A. To reduce the disulfide bonds of the thiolated single stranded DNA (ssDNA) to monothiol, 20 µL of 100 µM modified oligo was incubated with 20 µL of 10 mM (Tris (carboxyethyl) phosphine hydrochloride (TCEP) for 30 minutes at room temperature. Then, a solution of activated 1 µM thiol-labeled ssDNA oligo diluted in buffer A was flown into the channel and incubated overnight in the dark and at room temperature. After washing the channel with 100 µL of buffer A, a solution of 1 mM 6-Mercapto-1-hexanol (MCH) was flown and incubated for 30 minutes. Finally, the sample was left in either buffer B or C (for femtosecond pulsed-laser irradiation or fluorescence imaging, respectively) after washing it with 100 µL of buffer B. For fluorescence microscopy imaging, a solution of the complementary imager strand diluted to the desired concentration in buffer C was flown into the channel immediately before

starting the measurements. DNA re-functionalization of the gold nanoantennas was performed by flowing a 1 μM solution of another type of activated thiol-labeled single stranded DNA oligo in buffer A and incubating for 2 hs at room temperature. The backfilling step with MCH was performed exactly as described previously. Selective attachment of gold nanoparticles to gold nano-arrays, was performed by first incubating the gold nano-arrays with a 1 mM solution of MCH for 30 minutes. Following selective desorption, the sample was immediately immerse in a 1 mM biotin-SAM solution for 1 hs and clean by sequential washing steps of ethanol and water. The sample was finally washed with 1 mM PBS buffer and left to react with a solution of 50 nm streptavidin functionalized gold nanoparticles of OD=1 overnight. The solution of nanoparticles was removed and the sample was washed with 1 mM PBS buffer several times before SEM imaging.

Fluorescence microscopy imaging. Fluorescence imaging was carried out on a custom-built total internal reflection fluorescence microscope, based on an inverted Nikon Eclipse Ti-U microscope (Nikon Instruments) and equipped with an oil-immersion TIRF objective (Apo DIC N2 TIRF 100×, numerical aperture (NA) 1.49, oil). The effective pixel size is of 160 nm. Fluorescence excitation was at 640 nm using a 20 mW CW laser (LDH, Picoquant) spectrally filtered with a clean-up filter (BrightLine HC 636/8, Semrock). The laser was coupled into the microscope objective using a single-edge dichroic beam splitter (BrightLine FF 649, Semrock) and focused on the back focal plane of the objective aligned for TIRF illumination. Fluorescence light was spectrally filtered using an emission filter (ET705/72m, Chroma Technology) and imaged on an electron-multiplying charge-coupled device (EMCCD) camera (Evolve 512 Delta, Photometrics). For DNA-PAINT measurements, 20,000 frames per super-resolution image were recorded at a frame rate of 10Hz and at an excitation intensity of ~ 450 W cm^{-2}. The CCD

readout bandwidth was set to 5 MHz at 16 bits and 3 pre-amp gain. The electron multiplying (EM) gain was set at 200. Imaging conditions were as follows. The concentration of the imager strand was determined empirically to guarantee biding of only one single imager strand per diffraction limited-area.

Super-resolution data processing and image analysis. Super-resolution images were reconstructed from the raw data based on subsequent localization of single molecules *via* sparse segmentation and Gaussian fitting using the rainSTORM Matlab application presented in Supporting Reference 13. Prior single molecule localization, stage drift correction and background subtraction of the photoluminescence (static, auto-fluorescence emission) from the gold nanoantennas were performed with an in-house Matlab routine. Specifically, an efficient subpixel image registration algorithm based on cross-correlation was used for drift correction to within 1/10 of a pixel precision. This algorithm is referred to as the single-step DFT algorithm in Supporting Reference 14. Background subtraction was performed using the average image of the drift-corrected image stack, which reduces the static background gold luminescence without masking the detection of the fluorescent single molecule binding events. Images of individual gold nanoantennas were typically reconstructed from 700 to 3,000 localizations. To reconstruct high-density super-resolution images of gold nanoantennas exposed to specific chemical and/or optical conditions, we overlaid super-resolution images of 28 to 36 individual gold nanoantennas that had been exposed to the same conditions. The alignment of the individual nanoantennas was possible by calculating the coordinates of the center of each nanoantenna with high accuracy. This was performed using a translation registration algorithm (Matlab built-in function), which estimates the geometric transformation that aligns an image with a fixed template. The template was design according to the shape and dimension of each type of fabricated nanoantenna.

Femtosecond pulsed-laser irradiation. Selective desorption of thiol-modified oligos from gold nanoantennas was performed in a home-built optical set up which is based on a Nikon Eclipse Ti-U microscope (Nikon Instruments) that combines raster scanning of a sample with femto-second pulsed laser irradiation, together with, white light illumination and detection using a CCD camera (QICAM Fast 1394, QImaging). This configuration enables the automation and live monitoring of the single nanoantennas irradiation. Femtosecond pulsed-laser irradiation of individual nanoantennas was carried out using a collinear optical parametric amplifier (ORPHEUS, Light Conversion Ltd.) pumped by a femtosecond Ytterbium based laser system (PHAROS, Light Conversion Ltd.) operating at 100 kHz and with a pulse duration of ~180 fs. The excitation wavelength was set either to 820, 950 or 1100 nm and the beam polarization was adjusted with a half-wave plate and a polarizer. Note that the irradiation wavelengths in our experiments are far from the absorption wavelengths of DNA bases, avoiding any kind of direct photo-excitation process in the DNA-docking strands. The laser was coupled into the microscope objective (CFI S Plan Fluor ELWD 40×, NA 0.60, air) with a short-pass dichroic mirror of either 805 (DNSP805, Thorlabs) or 1000 nm (DMSP1000, Thorlabs), respectively, and focused onto the sample. The sample was fixed to an XYZ piezo-scanner stage (Nano-Drive, Mad City Laboratories) to perform the scanning. Each nanoantenna was irradiated for 10 seconds at power densities from 9 to 526 W/cm^2. Following irradiation, a washing step consisting of at least three washes using 100 μL of buffer B was performed.

Theoretical simulations. Theoretical calculations of the scattering/absorption cross-section spectra and the near-field intensity distributions were performed using both Lumerical FDTD 2017a and Comsol Multiphysics v4.4. The photo-thermal heating of gold nanoantennas for femtosecond laser irradiation was studied by coupling the Radio Frequency module with the

Heat Transfer module in Comsol. A dual-hyperbolic two-temperature model was adapted to study optical losses and their decay into the surrounding media (see Supporting Materials and Methods). The temperature dependent parameters of gold, glass, and water were taken from the Comsol material library.

Solution experiments for capping displacement. Citrate-capped 50 nm Au spherical nanoparticles OD=1 (AuNPs) and 150×50 nm^2 Au nanorods OD=1 (AuNRs) were modified with 1 mM 4-mercaptobenzoic acid (MBA) aqueous solution for 2 hours. The nanoparticles were later purified by two centrifugation steps at 4,000 rpm for 10 minutes and re-dispersed in water. Illumination of the colloidal mix (1:1 ratio) was performed in a quartz cuvette (3 ml total volume) under magnetic stirring conditions. Samples were irradiated at 780 nm for 10 minutes at 10 mW average power using the femtosecond laser previously described. Further increase on the irradiation time or power leads to AuNRs deformation as described in Supporting Reference 15. For SEM imaging quartz substrates were modified with APTES (5% in ethanol) for 1 hour followed by vigorous rising with ethanol. The solution containing the irradiated and non-irradiated nanoparticles were left overnight in a home-made humidity chamber. Many washing steps with water and final nitrogen drying were performed before SEM imaging.

ASSOCIATED CONTENT

Supporting Information. The Supporting Information is available free of charge on the ACS Publications website.

Surface coverage and electrochemical measurements, dual-hyperbolic two-temperature model, surface coverage estimation from electrochemical measurements, sorting and purification of colloidal nanoparticles, super resolution m-PAINT imaging of gold nanostructures, localization

precision and cross-sectional histograms, plasmonic response of gold nanotrimer structures, super-resolution m-PAINT imaging of thiol-desorption and ligand replacement from individual gold nanotrimer structures, controlling thiol-desorption and ligand replacement from gold nanotrimer structures with polarized light illumination, plasmonic response of six-leg gold nanostructures, plasmonic response of 'ICL' gold nanostructures, plasmonic response of 'L' gold nanostructures, numerical calculation of temperature profiles of plasmon-selective Au-S desorption on gold nanotrimers, solution-based sorting of metal nanoparticles, metallic DNA-PAINT docking and imager sequences.

The authors declare no competing financial interest

AUTHOR INFORMATION

Corresponding Author

*E-mail: s.simoncelli@imperial.ac.uk.

Author Contributions

‡These authors contributed equally.

Acknowledgments

This work has been supported by the EPSRC through the Reactive Plasmonics Programme (EP/M013812/1), the Royal Society, and the Lee-Lucas Chair in Physics. E.C. acknowledge financial support from the European Commission through a Marie Curie fellowship.

References

(1) Whitesides, G. M. Self-Assembly at All Scales. *Science* **2002**, *295*, 2418–2421.

(2) Ross, M. B.; Ku, J. C.; Vaccarezza, V. M.; Schatz, G. C.; Mirkin, C. A. Nanoscale Form Dictates Mesoscale Function in Plasmonic DNA–Nanoparticle Superlattices. *Nat. Nanotechnol.* **2015**, *10*, 453–458.

(3) Pensa, E.; Cortés, E.; Corthey, G.; Carro, P.; Vericat, C.; Fonticelli, M. H.; Benítez, G.; Rubert, A. A.; Salvarezza, R. C. The Chemistry of the Sulfur-Gold Interface: In Search of a Unified Model. *Acc. Chem. Res.* **2012**, *45*, 1183–1192.

(4) Häkkinen, H. The Gold–Sulfur Interface at the Nanoscale. *Nat. Chem.* **2012**, *4*, 443–455.

(5) Villarreal, E.; Li, G. G.; Zhang, Q.; Fu, X.; Wang, H. Nanoscale Surface Curvature Effects on Ligand-Nanoparticle Interactions: A Plasmon-Enhanced Spectroscopic Study of Thiolated Ligand Adsorption, Desorption, and Exchange on Gold Nanoparticles. *Nano Lett.* **2017**.

(6) Love, J. C.; Estroff, L. A.; Kriebel, J. K.; Nuzzo, R. G.; Whitesides, G. M. Self-Assembled Monolayers of Thiolates on Metals as a Form of Nanotechnology. *Chem. Rev.* **2005**, *105*, 1103–1169.

(7) Kumar, A.; Whitesides, G. M. Features of Gold Having Micrometer to Centimeter Dimensions Can Be Formed through a Combination of Stamping with an Elastomeric Stamp and an Alkanethiol “ink” followed by Chemical Etching. *Appl. Phys. Lett.* **1993**, *63*, 2002–2004.

(8) Shadnam, M. R.; Kirkwood, S. E.; Fedosejevs, R.; Amirfazli, a. Direct Patterning of Self-Assembled Monolayers on Gold Using a Laser Beam. *Langmuir* **2004**, *20*, 2667–2676.

(9) Tender, L. M.; Worley, R. L.; Fan, H.; Lopez, G. P. Electrochemical Patterning of Self-Assembled Monolayers onto Microscopic Arrays of Gold Electrodes Fabricated by Laser Ablation. *Langmuir* **1996**, *12*, 5515–5518.

(10) Hong, S. H.; Mirkin, C. A. A Nanoplotter with Both Parallel and Serial Writing Capabilities. *Science* **2000**, *288*, 1808–1811.

(11) Goodman, A. M.; Hogan, N. J.; Gottheim, S.; Li, C.; Clare, S. E.; Halas, N. J. Understanding Resonant Light-Triggered DNA Release from Plasmonic Nanoparticles. *ACS Nano* **2017**, *11*, 171–179.

(12) Jain, P. K.; Qian, W.; El-Sayed, M. A. Ultrafast Cooling of Photoexcited Electrons in Gold Nanoparticle-Thiolated DNA Conjugates Involves the Dissociation of the Gold-Thiol Bond. *J. Am. Chem. Soc.* **2006**, *128*, 2426–2433.

(13) Christopher, P.; Xin, H.; Linic, S. Visible-Light-Enhanced Catalytic Oxidation Reactions on Plasmonic Silver Nanostructures. *Nat. Chem.* **2011**, *3*, 467–472.

(14) Knight, M. W.; Sobhani, H.; Nordlander, P.; Halas, N. J. Photodetection with Active Optical Antennas. *Science* **2011**, *332*, 702–704.

(15) Jack, C.; Karimullah, A. S.; Tullius, R.; Khorashad, L. K.; Rodier, M.; Fitzpatrick, B.; Barron, L. D.; Gadegaard, N.; Lapthorn, A. J.; Rotello, V. M.; Cooke, G.; Govorov, A. O.; Kadodwala, M. Spatial Control of Chemical Processes on Nanostructures through Nano-Localized Water Heating. *Nat. Commun.* **2016**, *7*, 10946.

(16) Mubeen, S.; Lee, J.; Singh, N.; Krämer, S.; Stucky, G. D.; Moskovits, M. An Autonomous

Photosynthetic Device in Which All Charge Carriers Derive from Surface Plasmons. *Nat. Nanotechnol.* **2013**, *8*, 247–251.

(17) Linic, S.; Aslam, U.; Boerigter, C.; Morabito, M. Photochemical Transformations on Plasmonic Metal Nanoparticles. *Nat. Mater.* **2015**, *14*, 567–576.

(18) Brongersma, M. L.; Halas, N. J.; Nordlander, P. Plasmon-Induced Hot Carrier Science and Technology. *Nat. Nanotechnol.* **2015**, *10*, 25–34.

(19) Cortés, E.; Xie, W.; Cambiasso, J.; Jermyn, A. S.; Sundararaman, R.; Narang, P.; Schlücker, S.; Maier, S. A. Plasmonic Hot Electron Transport Drives Nano-Localized Chemistry. *Nat. Commun.* **2017**, *8*, 14880.

(20) De Nijs, B.; Benz, F.; Barrow, S. J.; Sigle, D. O.; Chikkaraddy, R.; Palma, A.; Carnegie, C.; Kamp, M.; Sundararaman, R.; Narang, P.; Scherman, O. A.; Baumberg, J. J. Plasmonic Tunnel Junctions for Single-Molecule Redox Chemistry. *Nat. Commun.* **2017**, *8*, 994.

(21) Roller, E.-M.; Besteiro, L. V.; Pupp, C.; Khorashad, L. K.; Govorov, A. O.; Liedl, T. Hotspot-Mediated Non-Dissipative and Ultrafast Plasmon Passage. *Nat. Phys.* **2017**, *13*, 761–765.

(22) Zewail, A. H. Femtochemistry: Atomic-Scale Dynamics of the Chemical Bond. *J. Phys. Chem. A* **2000**, *104*, 5660–5694.

(23) Petek, H. Photoexcitation of Adsorbates on Metal Surfaces: One-Step or Three-Step. *J. Chem. Phys.* **2012**, *137*, 91704.

(24) Yates, J. T.; Petek, H. Introduction: Photochemistry and Photophysics on Surfaces. *Chem. Rev.* **2006**, *106*, 4113–4115.

(25) Boerigter, C.; Aslam, U.; Linic, S. Mechanism of Charge Transfer from Plasmonic Nanostructures to Chemically Attached Materials. *ACS Nano* **2016**, *10*, 6108–6115.

(26) Zhang, X.; Li, X.; Zhang, D.; Su, N. Q.; Yang, W.; Everitt, H. O.; Liu, J. Product Selectivity in Plasmonic Photocatalysis for Carbon Dioxide Hydrogenation. *Nat. Commun.* **2017**, *8*, 14542.

(27) Cortés, E. Efficiency and Bond Selectivity in Plasmon-Induced Photochemistry. *Adv. Opt. Mater.* **2017**, *5*, 1700191.

(28) Jungmann, R.; Steinhauer, C.; Scheible, M.; Kuzyk, A.; Tinnefeld, P.; Simmel, F. C. Single-Molecule Kinetics and Super-Resolution Microscopy by Fluorescence Imaging of Transient Binding on DNA Origami. *Nano Lett.* **2010**, *10*, 4756–4761.

(29) Jungmann, R.; Avendaño, M. S.; Woehrstein, J. B.; Dai, M.; Shih, W. M.; Yin, P. Multiplexed 3D Cellular Super-Resolution Imaging with DNA-PAINT and Exchange-PAINT. *Nat. Methods* **2014**, *11*, 313–318.

(30) Peeters, S.; Stakenborg, T.; Reekmans, G.; Laureyn, W.; Lagae, L.; Van Aerschot, A.; Van Ranst, M. Impact of Spacers on the Hybridization Efficiency of Mixed Self-Assembled DNA/alkanethiol Films. *Biosens. Bioelectron.* **2008**, *24*, 72–77.

(31) Anger, P.; Bharadwaj, P.; Novotny, L. Enhancement and Quenching of Single-Molecule Fluorescence. *Phys. Rev. Lett.* **2006**, *96*, 113002.

(32) Khatua, S.; Paulo, P. M. R.; Yuan, H.; Gupta, A.; Zijlstra, P.; Orrit, M. Resonant Plasmonic Enhancement of Single-Molecule Fluorescence by Individual Gold Nanorods. *ACS Nano* **2014**, *8*, 4440–4449.

(33) Herne, T. M.; Tarlov, M. J. Characterization of DNA Probes Immobilized on Gold Surfaces. *J. Am. Chem. Soc.* **1997**, *119*, 8916–8920.

(34) Raab, M.; Vietz, C.; Stefani, F. D.; Acuna, G. P.; Tinnefeld, P. Shifting Molecular Localization by Plasmonic Coupling in a Single-Molecule Mirage. *Nat. Commun.* **2017**, *8*, 13966.

(35) Mack, D. L.; Cortés, E.; Giannini, V.; Török, P.; Roschuk, T.; Maier, S. A. Decoupling Absorption and Emission Processes in Super-Resolution Localization of Emitters in a Plasmonic Hotspot. *Nat. Commun.* **2017**, *8*, 14513.

(36) Virk, M.; Xiong, K.; Svedendahl, M.; Käll, M.; Dahlin, A. B. A Thermal Plasmonic Sensor Platform: Resistive Heating of Nanohole Arrays. *Nano Lett.* **2014**, *14*, 3544–3549.

(37) Manjavacas, A.; Liu, J. G.; Kulkarni, V.; Nordlander, P. Plasmon-Induced Hot Carriers in Metallic Nanoparticles. *ACS Nano* **2014**, *8*, 7630–7638.

(38) Brown, A. M.; Sundararaman, R.; Narang, P.; Goddard, W. A.; Atwater, H. A. Nonradiative Plasmon Decay and Hot Carrier Dynamics: Effects of Phonons, Surfaces, and Geometry. *ACS Nano* **2016**, *10*, 957–966.

(39) Khurgin, J. B. How to Deal with the Loss in Plasmonics and Metamaterials. *Nat. Nanotechnol.* **2015**, *10*, 2–6.

(40) Baffou, G.; Quidant, R.; García De Abajo, F. J. Nanoscale Control of Optical Heating in Complex Plasmonic Systems. *ACS Nano* **2010**, *4*, 709–716.

(41) Boles, M. A.; Ling, D.; Hyeon, T.; Talapin, D. V. The Surface Science of Nanocrystals. *Nat. Mater.* **2016**, *15*, 141–153.

(42) Correa-Puerta, J.; Del Campo, V.; Henríquez, R.; Esaulov, V. A.; Hamoudi, H.; Flores, M.; Häberle, P. Unoccupied Interface and Molecular States in Thiol and Dithiol Monolayers. *Langmuir* **2017**, *33*, 12056–12064.

(43) Nakaya, M.; Shikishima, M.; Shibuta, M.; Hirata, N.; Eguchi, T.; Nakajima, A. Molecular-Scale and Wide-Energy-Range Tunneling Spectroscopy on Self-Assembled Monolayers of Alkanethiol Molecules. *ACS Nano* **2012**, *6*, 8728–8734.

(44) Rodríguez, L. M.; Gayone, J. E.; Sánchez, E. A.; Grizzi, O.; Blum, B.; Salvarezza, R. C.; Xi, L.; Woon, M. L. Gas Phase Formation of Dense Alkanethiol Layers on GaAs(110). *J. Am. Chem. Soc.* **2007**, *129*, 7807–7813.

(45) The percentage of desorption was calculated from the ratio between the number of single-molecule localizations in the horizontal rod and the average number of localizations from the remaining two other rods.

(46) Zhang, C.; Zhao, H.; Zhou, L.; Schlather, A. E.; Dong, L.; McClain, M. J.; Swearer, D. F.; Nordlander, P.; Halas, N. J. Al-Pd Nanodisk Heterodimers as Antenna-Reactor Photocatalysts. *Nano Lett.* **2016**, *16*, 6677–6682.

(47) Reimers, J. R.; Ford, M. J.; Marcuccio, S. M.; Ulstrup, J.; Hush, N. S. Competition of van

Der Waals and Chemical Forces on Gold–Sulfur Surfaces and Nanoparticles. *Nat. Rev. Chem.* **2017**, *1*, 17.

(48) Boerigter, C.; Campana, R.; Morabito, M.; Linic, S. Evidence and Implications of Direct Charge Excitation as the Dominant Mechanism in Plasmon-Mediated Photocatalysis. *Nat. Commun.* **2016**, *7*, 10545.

(49) Xia, Y.; Xiong, Y.; Lim, B.; Skrabalak, S. E. Shape-Controlled Synthesis of Metal Nanocrystals: Simple Chemistry Meets Complex Physics? *Angew. Chem. Int. Ed.* **2009**, *48*, 60–103.

Figures

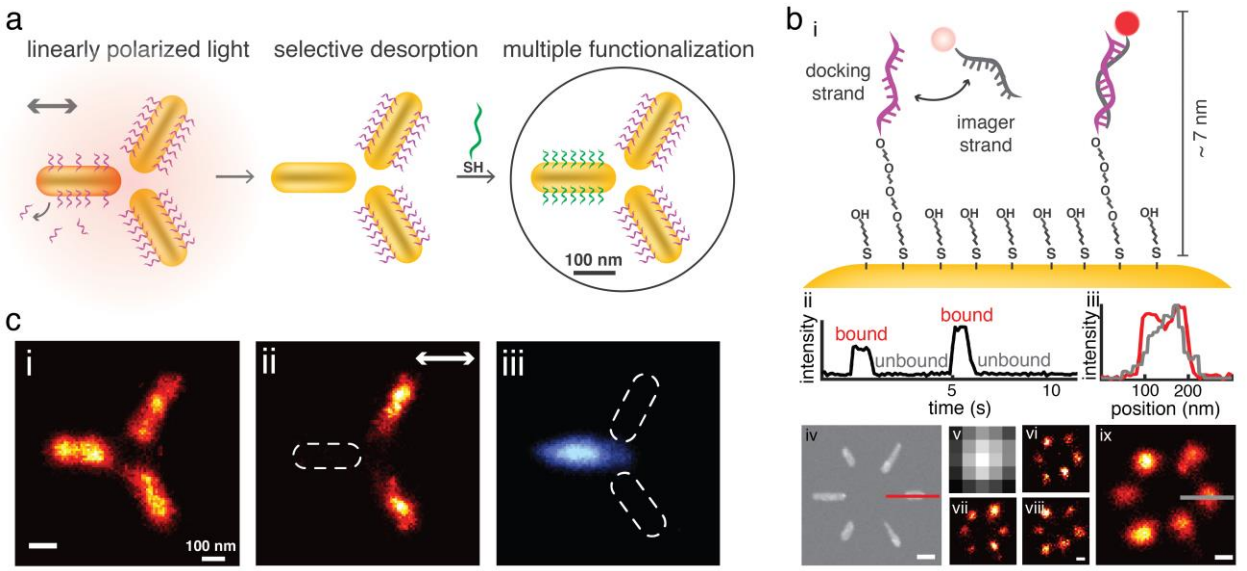

Figure 1. Plasmon-selective surface chemistry modification. (a) Optical excitation with a linearly polarized femtosecond pulsed laser enables selective and nano-localized molecular desorption of thiol-functionalized Au nanostructures. The unprotected region is now accessible for re-functionalization with a different thiol-reactive probe. **(b)** Super-resolution metallic DNA-PAINT imaging technique (i). Transient binding of fluorescently labeled DNA ('imager') strands to their complementary sequence ('docking') strands are detected as a switching between a dark (unbound) and a bright (bound) state (ii). SEM (iv), diffraction-limited (v) and super-resolved m-PAINT images (vi - viii) of individual Au six-leg nanostructures. Spatial intensity profile of the SEM (red) and the average super-resolved six-leg image (grey) along the horizontal short leg of the nanostructure (iii). Average super-resolution image (x) of 36 individual six-leg Au nanostructures (see Figure S2). **(c)** Average super-resolved m-PAINT images of 28 individual Au nanotrimers before (i) and after (ii, iii) irradiation with a 950 nm linearly polarized femtosecond pulsed laser (1.7 mJ/cm^2) and re-functionalization with the thiol-reactive docking strand P_2 (iii). Pseudo-colors red and blue for docking strands P_1 and P_2, respectively. The mean

number of localizations in individual images is 1,608 ± 564, 776 ± 480 and 1,080 ± 597 for i to iii.

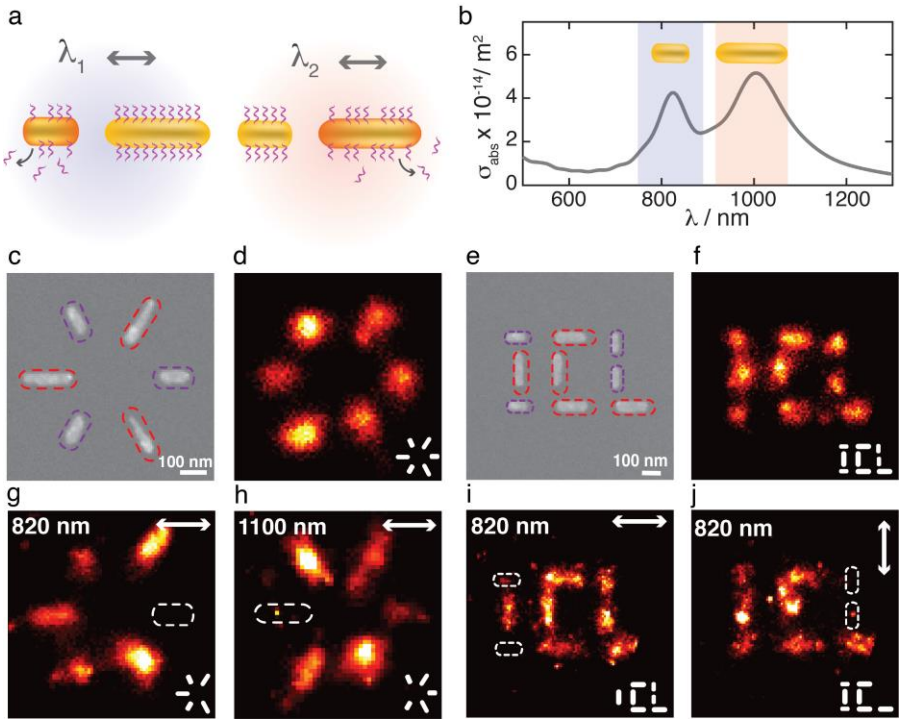

Figure 2. Wavelength and polarization control of thiol-desorption. (**a**) The spectral differences between nanorods that share the same orientation allow tuning the surface chemistry of packed nanostructures. (**b**) FDTD-simulated single-antenna absorption spectra of a two-leg Au nanostructure (dimensions: 170×50 nm^2, 110×45 nm^2, gap 120 nm). (**c**, **e**) SEM image of a six-leg or a custom-design letter pattern ('ICL') Au nanostructure composed of two sizes of nanorods with dimensions of 110×45 nm^2 (violet dashed line) and 170×50 nm^2 or 180×40 nm^2 (red dashed line) for the ICL and the six-leg nanostructure, respectively. (**d**, **f**, **g-j**) Average super-resolved m-PAINT images of 35 individual Au nanostructures functionalized with docking strand P_1 before (**d**, **f**) and after (**g-j**) irradiation with a 820 nm (**g**, **i**, **j**) or a 1100 nm (**h**) linearly polarized femtosecond pulsed laser of 1.9 mJ/cm^2 (**g**) or 2.6 mJ/cm^2 (**i**, **j**) or 3.8 mJ/cm^2 (**h**) fluence. White arrows represent the polarization of the incident light. The mean number of

localizations in individual images is 1,458 ± 332; 1,579 ± 351; 1931 ± 672; 1,580 ± 496; 970 ± 384 and 689 ± 263 for (**d**, **f-j**), respectively.

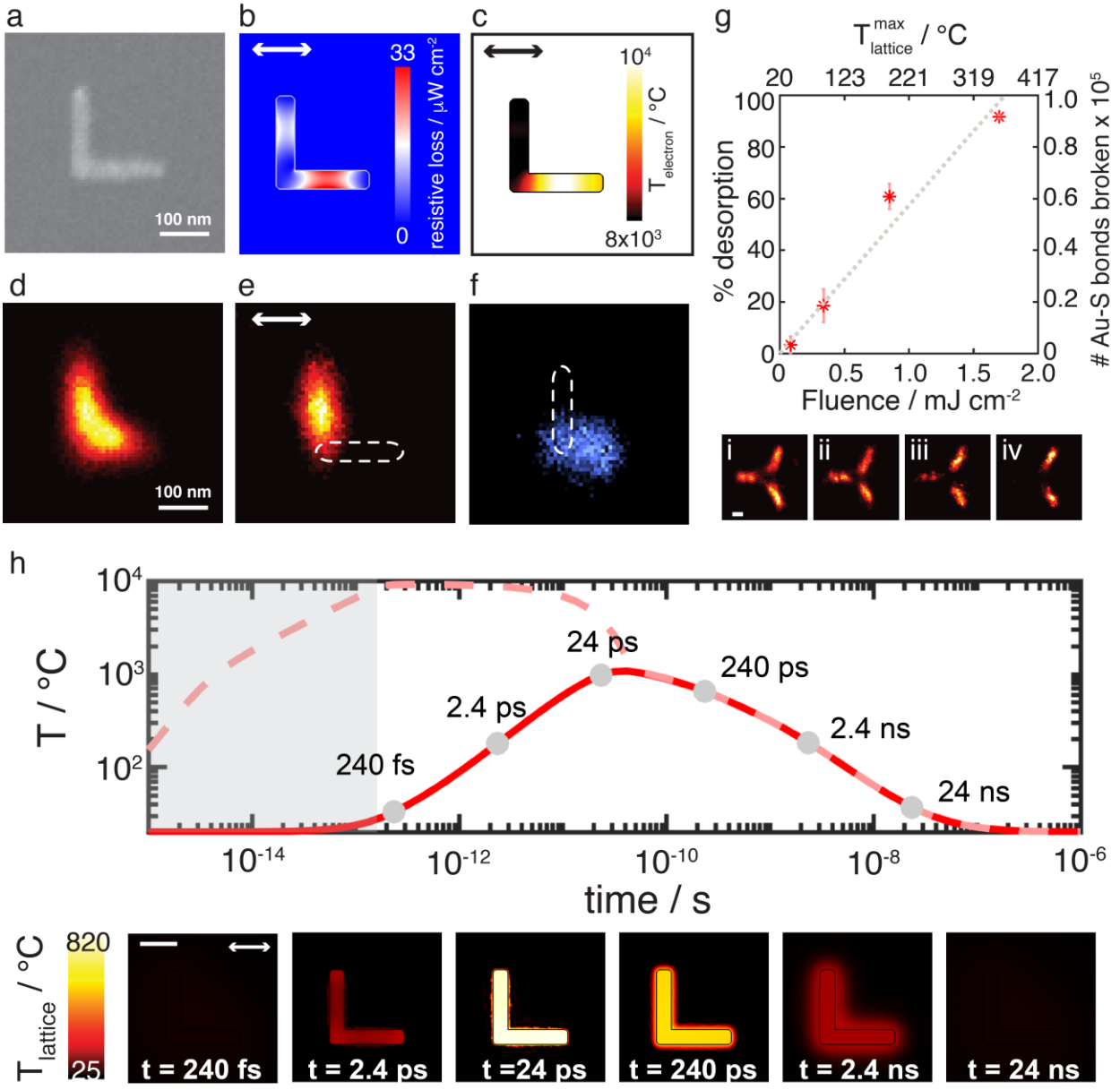

Figure 3. Plasmon-selective Au-S desorption mechanism. (**a**) SEM image of an L-shape Au nanostructure. (**b, c**) Resistive loss and electron temperature distribution at 240 fs delayed from the temporal start of a 180 fs laser pulse (950 nm, 5.3 mJ/cm^2). (**d-f**) Average super-resolved m-

PAINT images (n = 31) before (**d**) and after (**e**, **f**) irradiation (950 nm, 5.3 mJ/cm^2) and re-functionalization (**f**) with the thiol-reactive docking strand P_2. The mean number of localizations is 2,016 ± 380, 701 ± 436 and 260 ± 202 for **d** to **f**. (**g**) Power dependent Au-S desorption of docking strand P_1 from Au nanotrimers after femtosecond pulse irradiation (0°, 950 nm). Error bars correspond to the average of two independent data sets. The dashed grey line corresponds to the linear fit of the data (R^2 = 0.96). i-iv, Average super-resolved m-PAINT images (n = 31) of nanotrimers after laser irradiation of 0.08, 0.3, 0.6 and 1.7 mJ/cm^2 fluence, respectively. The mean number of localizations is 2,764 ± 804, 1,586 ± 621, 1,157 ± 463 and 776 ± 480 for i to iv. (**h**) Simulated temporal evolution of the electron temperature (dashed line) and lattice temperature (full line) following femtosecond laser irradiation. Map distribution of the lattice temperature at different delays after the temporal start of the fs laser pulse.

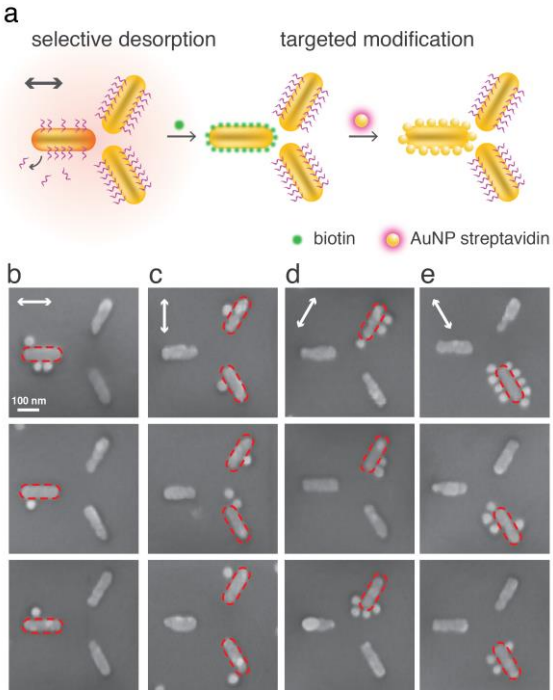

Figure 4. Hierarchical assembly of metal nanostructures (**a**) Au nanostructures are first modified with a self-assembly monolayer of 6-mercapto-1-hexanol and then illuminated with a linearly polarized femtosecond laser at their local surface plasmon resonance wavelength (950 nm, 1.7 mJ/cm^2). The samples are rinsed and immediately functionalized with a biotin terminal group. Streptavidin coated Au nanoparticles (50 nm) are then left to react overnight with the bi-functionalized Au nanostructures. SEM images are acquired after several washing steps with PBS buffer. (**b-e**) Representative SEM images of the 50 nm Au nanoparticles binding to the fabricated bi-functionalized gold nanostructures. White arrows represent the polarization of the incident light.

Graphical Table of Contents (TOC)